

Robust excitation of C-band quantum dots for enhanced quantum communication

Michal Vyvlecka,^{1,*} Lennart Jehle,^{1,*} Cornelius Nawrath,² Francesco Giorgino,¹ Mathieu Bozzio,³ Robert Sittig,² Michael Jetter,² Simone L. Portalupi,² Peter Michler,² and Philip Walther^{3,4}

¹ University of Vienna, Faculty of Physics & Vienna Doctoral School in Physics & Vienna Center for Quantum Science and Technology, Boltzmanngasse 5, A-1090 Vienna, Austria

² Institut für Halbleiteroptik und Funktionelle Grenzflächen, Center for Integrated Quantum Science and Technology (IQST) and SCoPE, University of Stuttgart, Allmandring 3, 70569 Stuttgart, Germany

³ Vienna Center for Quantum Science and Technology,

Faculty of Physics, University of Vienna, Vienna, Austria

⁴ Christian Doppler Laboratory for Photonic Quantum Computer, Faculty of Physics, University of Vienna, Vienna, Austria

(Dated: May 23, 2023)

Building a quantum internet requires efficient and reliable quantum hardware, from photonic sources to quantum repeaters and detectors, ideally operating at telecommunication wavelengths. Thanks to their high brightness and single-photon purity, quantum dot (QD) sources hold the promise to achieve high communication rates for quantum-secured network applications. Furthermore, it was recently shown that excitation schemes, such as longitudinal acoustic phonon-assisted (LA) pumping, provide security benefits by scrambling the coherence between the emitted photon-number states. In this work, we investigate further advantages of LA-pumped quantum dots with emission in the telecom C-band as a core hardware component of the quantum internet. We experimentally demonstrate how varying the pump energy and spectral detuning with respect to the excitonic transition can improve quantum-secured communication rates and provide stable emission statistics regardless of network-environment fluctuations. These findings have significant implications for general implementations of QD single-photon sources in practical quantum communication networks.

I. INTRODUCTION

The emergence of practical quantum technology paves the way to a quantum internet – a network of connected quantum computers capable of reaching computational speed-ups in various tasks such as prime factoring [1], machine learning [2] and the verification of NP-complete problems with limited information [3]. Although such schemes are appealing, most are technologically challenging, while the security advantages provided by quantum networks are more tangible [4–6]. A broad range of quantum-cryptographic primitives including quantum key distribution (QKD) [4–6], quantum coin flipping [7–9], unforgeable quantum tokens [10–12], and quantum bit commitment [13–15] have been developed to demonstrate some security advantage over their classical counterparts. The success of a future quantum internet then relies on the development of fundamental quantum hardware (sources, repeaters and detectors) which should adhere to these primitives’ security standards, provide high communication rates, and operate reliably in a real-world environment [16].

Non-classical light sources such as spontaneous parametric down-conversion [17, 18], nitrogen-vacancy centers [19] and trapped atoms [20], have been used as hardware for the first quantum networks. In recent years,

semiconductor quantum dots (QDs) have materialized as highly versatile and quality single-photon sources [21–25], with outstanding end-to-end efficiencies overcoming 57% and the potential to reach repetition rates of tens of GHz [24]. The outstanding emission properties of QDs have lead to the implementation of complex network building blocks relying on quantum teleportation [26, 27] and quantum entanglement swapping [22, 23, 28]. Regarding the emission wavelength, the spectral regime of the telecom C-band (1530 nm to 1565 nm) is highly appealing, due to its global absorption minimum in standard silica fibers, the possibility to implement daylight satellite communication [29] and the compatibility with the mature silicon photonic platforms [30]. QDs with emission wavelengths in and around the C-band are available on indium phosphide (InP) [31–33] and gallium arsenide (GaAs) material system [34–36], and circumvent the technical overhead and losses of quantum frequency conversion [37]. Embedded in circular Bragg cavities, QDs based on the low-cost and well-established GaAs platform have simultaneously demonstrated high brightness and high purity values recently [36].

Previous works have investigated the advantages and drawbacks of various optical pumping schemes (resonant, phonon-assisted and two-photon excitation) in terms of efficiency, single-photon purity and indistinguishability [38–40]. On the other hand, it was recently shown that such schemes must be carefully tuned to satisfy the security assumptions of each quantum-cryptographic application [41]. Crucially, quantum coherences between the emitted photon-number components must be scram-

* These authors contributed equally: Michal Vyvlecka, Lennart Jehle. Address all correspondence to michal.vyvlecka@univie.ac.at, lennart.jehle@univie.ac.at

bled for optimal performance, which is inherently provided by longitudinal phonon-assisted (LA) excitation. On top of their intrinsic security benefits, LA schemes are fairly insensitive to pump instabilities like power or polarization fluctuations, making them suitable for QDs in real-life communication networks [38, 39]. Furthermore, such schemes do not require challenging single-photon polarization filtering (contrary to the resonant counterpart), and thus promise an experimentally straightforward way to obtain simultaneously high brightness and purity [38].

In this work, we combine all aforementioned advantages implementing LA excitation in the C-band, and exploit its tunable parameters to investigate the complex dependence of brightness and purity on pump pulse energy and spectral detuning. We relate this non-trivial behavior to the security properties of single-photon quantum key distribution (QKD), and show how the optimal operation conditions are dependent on the length of the communication fiber link. In agreement with theoretical findings [42], our results show that, unlike its resonant and two-photon counterparts, the characteristics of LA excitation can be tuned to achieve the ideal photon-number statistics. This optimization is reminiscent of the mean-photon adjustment required in weak coherent state (WCS) implementations [43].

II. EXCITATION PARAMETER INVESTIGATION

Most quantum-secured applications rely on few trusted parameters that are typically not all experimentally accessible. Here, we infer the photon-number probabilities $\{p_k\}$ from two measurements, the brightness $B = \sum_{k=1}^{\infty} p_k$ and the single-photon purity $P = 1 - g^{(2)}(0)$, where $g^{(2)}(0)$ is the second-order auto-correlation measurement evaluated at zero time delay. See Fig. 1 for an exemplary QD behaviour under LA excitation.

While scanning both the power and wavelength of the pulsed and mode-locked pump laser, we simultaneously measure the brightness B and single-photon purity P and compile the results in 2D maps as shown in Fig. 2 (a) and (b), respectively. Due to the low phonon density at a sample temperature of ~ 4 K we excite the investigated InAs QD only with positive detunings $\Delta = \hbar(\omega_{\text{laser}} - \omega_{\text{dot}}) > 0$. The brightness map features a single, broad maximum around $\Delta \approx 0.8$ meV ($\Delta\lambda \approx 1.5$ nm) agreeing with similar experimental findings [44, 45] and theoretical studies [46, 47]. LA excitation with sufficiently smooth pulses [48] achieves a population inversion of the QD ground and excited state if the effective Rabi splitting of the laser-dressed states, $\hbar\Omega_{\text{eff}} = \sqrt{(\hbar\Omega)^2 + \Delta^2}$, ensures an efficient exciton-phonon coupling that is characterized by the spectral phonon density $J(\omega)$ [44, 46]. The robustness of this scheme against power and wavelength fluctuations of the excitation laser is demonstrated

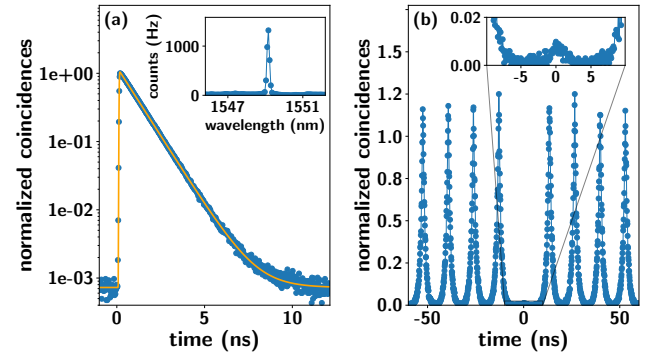


FIG. 1. **Characterization of the pulsed LA excitation of the positively charged exciton transition.** The InAs QD is based on an InGaAs metamorphic buffer layer with non-linearly graded In content enabling emission in the telecom C-band [35]. The excitation is provided by a tunable, mode-locked fiber laser with a pulse length of 17(1) ps and a spectral width of 210(20) pm. The QD transition line is filtered by a set of volume Bragg grating filters (FWHM=0.2 nm). The total setup efficiency is determined to 15 %. (a) Time-resolved fluorescence measurement in a semi-logarithmic scale. The mono-exponential fit function (solid line) yields a decay time of 1.07(2) ps. The inset shows a micro photoluminescence (μ -PL) spectrum of the studied transition, including spectral suppression of the laser with an excitation power of 41 μ W and a detuning of 1.5 nm from the QD resonance. (b) Second-order auto-correlation measurement $g^{(2)}(\tau)$ for an excitation power of 11 μ W and a detuning of 1.1 nm. The well suppressed peak at zero time delay confirms the high single-photon purity ($g^{(2)}(0) = 0.018(1)$). Further details on the analysis of $g^{(2)}(0)$ can be found in Appendix B.

by the broad maximum of the brightness in Fig. 2 (a) and stems from the spectral width of $J(\omega)$. Thus, the large bandwidth of the phonon interaction directly benefits a stable operation of the QD source. Only for large detunings and weak fields, the phonon-induced relaxation to the exciton level fails and the brightness drops significantly. Similarly, for high powers, the effective Rabi splitting is no longer in resonance with the phonon interaction resulting in reduced brightness.

Besides emission efficiency, the single-photon purity of the quantum-light source is crucial to the performance of cryptographic protocols [41]. Therefore, we analyze the purity P , depicted in Fig. 2 (b), for the same parameter range as the brightness. We identify a broad region of high purity at similar detunings but shifted towards lower powers. At large detunings, the purity degrades because the exciton state preparation via LA phonons becomes less efficient (evident by the low brightness in the same area of Fig. 2 (a)) and spurious contributions to the emission, including neighboring QDs or a quasi-continuum of transitions, are no longer negligible. Considering a perfect two-level system, Ref. [42] predicts an enhanced purity for increasing pulse areas because the

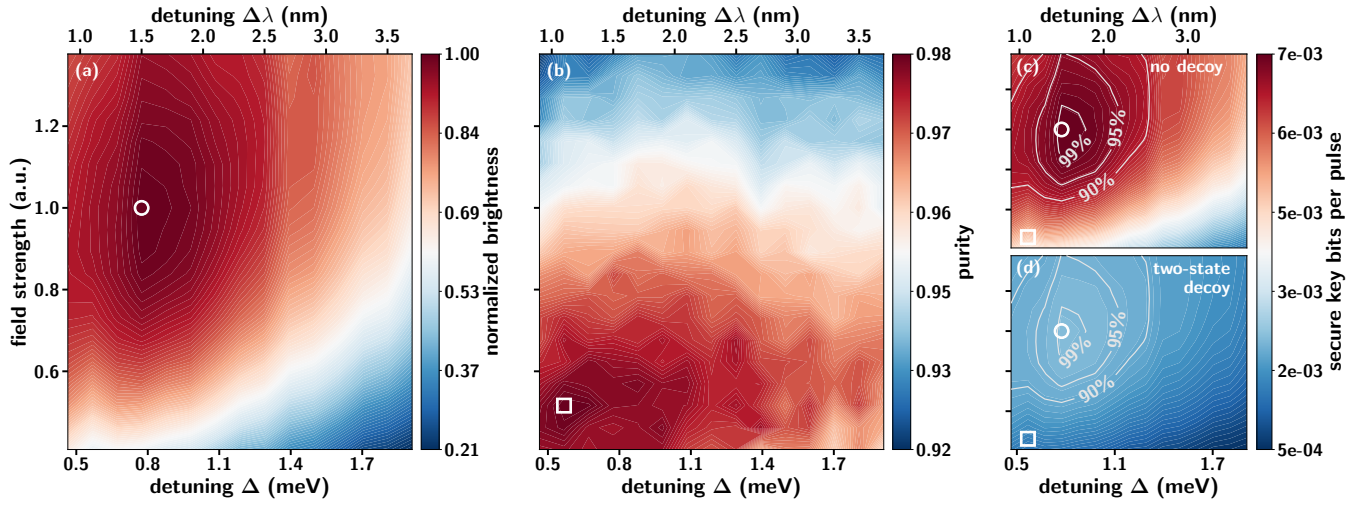


FIG. 2. Measured photon-number statistics and extrapolated QKD secure key bits per pulse for LA excitation. Scanning the excitation parameters while simultaneously measuring (a) brightness $B = \sum_{k=1}^{\infty} p_k$ and (b) single-photon purity $P = 1 - g^{(2)}(0)$ of the QD emission. The white circle (square) marks the set of excitation parameters achieving the optimal brightness (purity). From the photon-number populations $\{p_k\}$, the secure key bits per pulse (SK) are calculated for zero distance based on the BB84 QKD protocol without (c) and with two decoy states (d). For more details on the parameter estimation see Appendix C. The equipotential lines indicate where the SK has dropped to $\{99\%, 95\%, 90\%\}$ of their individual SK maxima. The SK was estimated in the asymptotic limit [49], $SK = \eta_{\text{sif}}[Q_1(1 - H_2(E_1)) - f(E)Q_{\text{tot}}H_2(E_{\text{tot}})]$, where H_2 is the binary Shannon entropy and $\eta_{\text{sif}} = 1/2$ for standard BB84, whereas $\eta_{\text{sif}} = 1/6$ for two-state decoy. Parameters for all plots are: single-photon detection error $e_d = 0.02$, detection efficiency $\eta_d = 0.86$, dark-count probability $Y_0 = 1.6 \cdot 10^{-6}$, error-correction code inefficiency $f = 1.2$.

phonon-induced level inversion is delayed until the end of the pulse. As a consequence, the chance of a reexcitation event during the same pulse, as it is known for resonant pumping [38, 50], would be reduced. In our experiment, however, this process competes with, and is eventually out-weighed by, the aforementioned unintended emission decreasing the purity at high powers significantly.

Interestingly, our experimental findings imply the absence of a trivial set of optimal parameters (simultaneously maximizing brightness and single-photon purity), which confirms some of the complex behaviours predicted in previous theory works [41, 42]. Instead, a careful tuning of the excitation parameters is required for each quantum-cryptographic application. Depending on the desired security of merit, the correct weighting of the photon-number populations $\{p_k\}$ used for the optimization [41] must be defined. At the same time, fluctuations in the excitation parameters produce only small changes in photon-number populations. Furthermore, optimal brightness and near-optimal purity are achieved for a pump pulse detuned by ≈ 1.5 nm from the QD transition that can be readily separated from the single-photon emission using efficient, off-the-shelf spectral filters. This removes the need for a cross-polarization setup simplifying the source's operation, optimizing usable brightness and further underlines the practicality of LA excitation for network applications [4–15]. In the following section, we experimentally show how to perform the excitation

parameter optimization on the example of quantum key distribution, arguably the best-known primitive in quantum communication.

III. QUANTUM KEY DISTRIBUTION (QKD)

QKD allows two parties to establish a secret key over an eavesdropped channel [4, 51]. In that sense, the most natural figure of merit is the number of secure bits communicated per round of the protocol. This quantity can be computed from two experimental parameters: the total gain Q_{tot} , corresponding to the probability of detecting at least one photon from a given pulse sent by Alice, and the total error rate E_{tot} , indicating the fraction of states for which the wrong (polarization) detector clicks. Naturally, only the error-free single photon states contribute positively to the secure key, while the multi-photon contribution p_m leaks significant amounts of information. Starting from experimental data, one therefore needs to estimate the values of the single-photon gain Q_1 and the single-photon error rate E_1 , which are not directly accessible. In Appendix C, we infer these quantities in two ways: first by deriving an upper bound on the multi-photon emission probability

$$p_m \leq \frac{1 - Bg^{(2)}(0) - \sqrt{1 - 2Bg^{(2)}(0)}}{g^{(2)}(0)} \quad (1)$$

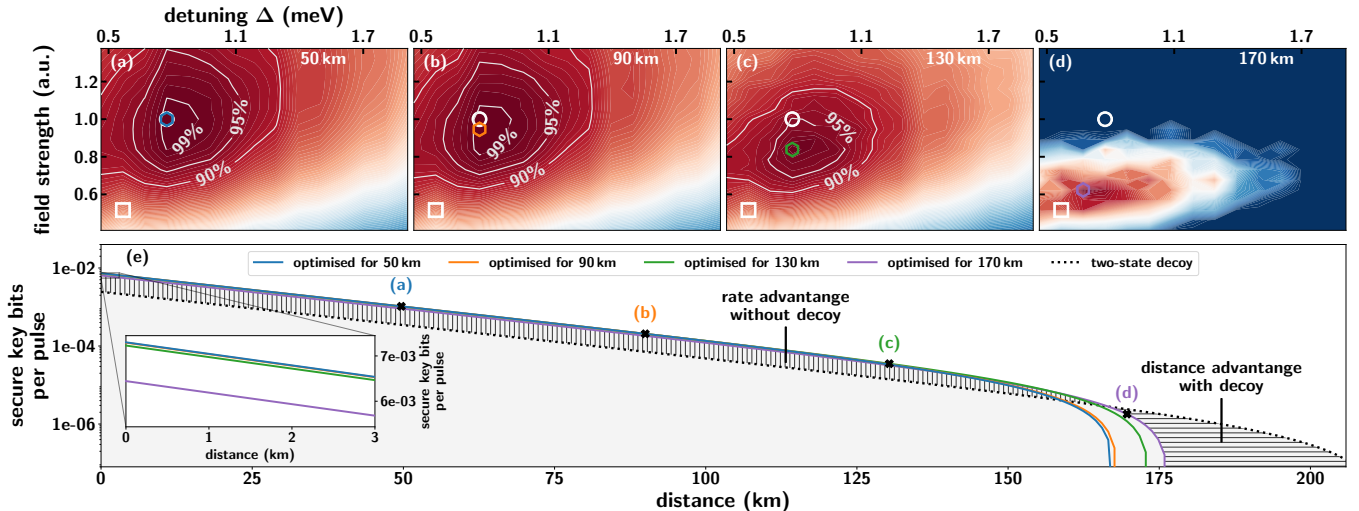


FIG. 3. Secure key rates of BB84 QKD for varying communication distances. Secure key bits per pulse for the LA excitation parameter space in a standard BB84 QKD scenario for increasing channel length $\{50 \text{ km}, 90 \text{ km}, 130 \text{ km}, 170 \text{ km}\}$ (a)-(d), where we assumed a fiber attenuation of $\alpha = 0.17 \text{ dB/km}$, typical for the telecom C-band. The white circle (square) marks the set of excitation parameters achieving the optimal brightness (purity) as shown in Fig. 2, whereas the colored hexagon marks the trade-off between the two, optimizing the SK at the given distance. The color scale of each maps is normalized to its maximum SK . (e) Calculating the SK for each highlighted parameter set from (a)-(d) as a function transmission loss demonstrates how the tunability of LA excitation helps to adapt the emission statistics to the channel. The two-state decoy protocol reduces the SK by a factor of ~ 3 at short and medium distances but performs better in the high-loss regime. The parameters used to calculate the SK are the same as for Fig. 2.

and second by employing the two-state decoy approach [52, 53]. Compared to previous work [54], Eq. 1 gives an explicit expression for p_m relying only on the experimentally accessible B and $g^{(2)}(0)$ and provides additional intuition to Ref. [55].

Following the parameter estimation, we calculate the attainable secure key bits per pulse (SK) for standard and decoy-state BB84 QKD for each set of excitation parameters as shown for zero communication distance in Fig. 2 (c) and (d), respectively. While the qualitative dependence of the SK is very similar for both protocols, the performance gap is evident in the absolute values. Even under the favorable assumption of a lossless amplitude modulator, the SK of the two-state decoy is ~ 3 smaller than for the standard BB84 protocol. Decoy states have been introduced to handle the risk of multi-photon contributions p_m , but since these are inherently small for QDs, replacing a portion of the signal states with decoy states outweighs the effect of an exact bounding of p_m . Furthermore, comparing Fig. 2 (a)-(c) shows that for zero distance the brightness (more accurately, p_1) dominates the SK map making a tight bounding of p_m even less relevant.

However, the impact of the multi-photon events on the SK comes into play for non-zero communication distances making the ideal set of $\{p_k\}$ no longer trivial but dependent on the channel loss. Computing SK maps at four distances, as depicted in Fig. 3 (a)-(d), visualizes the shift in source requirements. Short-distance trans-

missions benefit most from a bright source, whereas high-loss scenarios such as long-distance communication call for sources with high purity. Fig. 3 (e) then shows how these four ideal parameter sets behave over distances. The difference in performance underlines the potential of individually adjusting the excitation conditions with respect to the channel loss. Note that the joint optimization of $\{p_k\}$ by tuning the pump conditions is possible with resonant or two-photon excitation but less performant.

The maximum distance for which the generation of a secure key is still possible is of great interest for applications. Since there is no analytical expression, we state the maximal communication distance as minimal channel transmission η_{ch}^{\min} and find that the approximation

$$\eta_{\text{ch}}^{\min} \approx \frac{Bg^{(2)}(0)}{2} + Y_0, \quad (2)$$

where Y_0 is the dark-count probability, captures the break-down of secure key generation well under realistic assumptions. Due to its construction (effectively lower bounding η_{ch}^{\min}), Eq. 2 always overestimates the distance by $\sim 30 \text{ km}$ (see Appendix D). Eq. 2 also implies that, within the limits of the approximation, a brighter source reduces the maximum communication distance. Counter-intuitive at first sight, this is readily explained as the multi-photon probability p_m increases with the source brightness if $g^{(2)}(0)$ is unchanged (see Eq. 1). While brighter QDs further im-

prove the SK at short to medium distances, one must reduce the multi-photon component when communicating over large distances. For this purpose, simply attenuating the signal before launching it into the untrusted channel is sufficient. Note how this approach resembles the mean-photon number optimization used for QKD with WCS [43]. Considering a detector dark-count probability $Y_0 = 10^{-7}$, single-photon detection error $e_d = 0.02$ and a highly pure source ($g^{(2)}(0) = 0.02$), our numerical analysis (see Appendix D) identifies the ideal brightness for maximum distance as $B \approx 0.9\%$. This is well within range of today's telecom C-band QD-technology.

Finally, we remark that implementing decoy states can be advantageous in the long-distance regime even for highly pure single-photon sources such as QDs, as reflected in Fig. 3 (e). However, for low to moderate loss, standard BB84 outperforms the decoy-state protocol due to the larger sifting factor η_{sif} .

IV. DISCUSSION

In this work, we investigated the benefits that the phonon-assisted excitation of a telecom C-band QD provides for quantum-secured applications. In addition to the previously known absence of coherence in the photon-number basis [41], its robustness against environmental fluctuations [39] and ease of efficient single-photon filtering, we showed that LA excitation allows to effectively optimize the photon-number statistics with respect to the application. This feature originates from interaction with the phonon environment and is therefore not common to resonant excitation schemes but can be exploited by tailoring the LA pumping conditions. The complex implications of phonon interactions for brightness and single-photon purity have also been theoretically predicted for idealized systems [42]. Therefore, our observations can be generalized to other quantum-dot-based sources.

As a means of improving the emission statistics independent of the excitation mechanism, temporally filtering the signal was proposed [56, 57] but requires special hardware and comes at the prize of additional loss. Moreover, we show in Appendix E that optimizing $\{p_k\}$ using only the LA pump power is as efficient as time filtering with a fast and lossless modulator. Only at very large distances time filtering performs better because it also reduces the source brightness and detector dark counts.

However, we note that two-photon excitation can simultaneously yield a higher brightness and purity than achievable for any parameter set using the LA scheme [50]. Nevertheless, two-photon excitation – being a resonant process – is sensitive to environmental fluctuations, requires more pump power [58] if compared to LA and is thus less suitable for real-world implementations.

Furthermore, we found that even for quantum light sources with inherently low multi-photon contribution, decoy states can push the maximum attainable distance in QKD. Although, in consideration of the low SK at

these distances and the experimental overhead involved, we believe that decoy states are not beneficial for QD implementations.

Finally, we would like to stress that we optimized the photon-number statistics in LA excitation with respect to QKD as an example but the process is transferable to other quantum-secured applications and prone to improve their performance.

ACKNOWLEDGEMENTS

This research was funded in whole, or in part, from the European Union's Horizon 2020 and Horizon Europe research and innovation programme under grant agreement No 899368 (EPIQUS), the Marie Skłodowska-Curie grant agreement No 956071 (AppQInfo), and the QuantERA II Programme under Grant Agreement No 101017733(PhoMemtor); from the Austrian Science Fund (FWF) through [F7113] (BeyondC), and [FG5] (Research Group 5); from the Austrian Federal Ministry for Digital and Economic Affairs, the National Foundation for Research, Technology and Development, the Christian Doppler Research Association, the German Federal Ministry of Education and Research (BMBF) via the project QR.X (No.16KISQ013) and the European Union's Horizon 2020 research and innovation program under Grant Agreement No. 899814 (Quurope). Furthermore, this project (20FUN05 SEQUME) has received funding from the EMPIR programme co-financed by the Participating States and from the European Union's Horizon 2020 research and innovation programme.

For the purpose of open access, the author has applied a CC BY public copyright licence to any Author Accepted Manuscript version arising from this submission.

APPENDIX A: EXPERIMENTAL SETUP

The scheme of the experimental setup is displayed in Fig. A1. We use an Er-doped fiber pulsed mode-locked laser at a repetition rate of $\nu_{\text{rep}} = 75.95\text{ MHz}$ to excite the quantum dot (QD). A filter with 1 nm bandwidth inside the laser cavity stretches the generated pulses to a pulse width of 10.1 ps (spectral width FWHM 0.4 nm, the pulses are not Fourier-limited). The laser provides tunability of wavelength between 1530 nm and 1550 nm at an average output power 200 mW. The laser pulses are then stretched by a free space pulse shaper in 4-f, which is based on a reflective grating (1200 lines/mm, blase at 1550 nm) with efficiency $\approx 90\%$, C-coated lens with a focal length of 400 nm and tunable filtering slit. The pulses after the pulse shaper have a pulse width of 17(1) ps.

The pulse-shaped excitation laser beam is coupled to single-mode fiber and then collimated by an 8 mm lens collimator. A Glan-Taylor polarizer sets the excitation

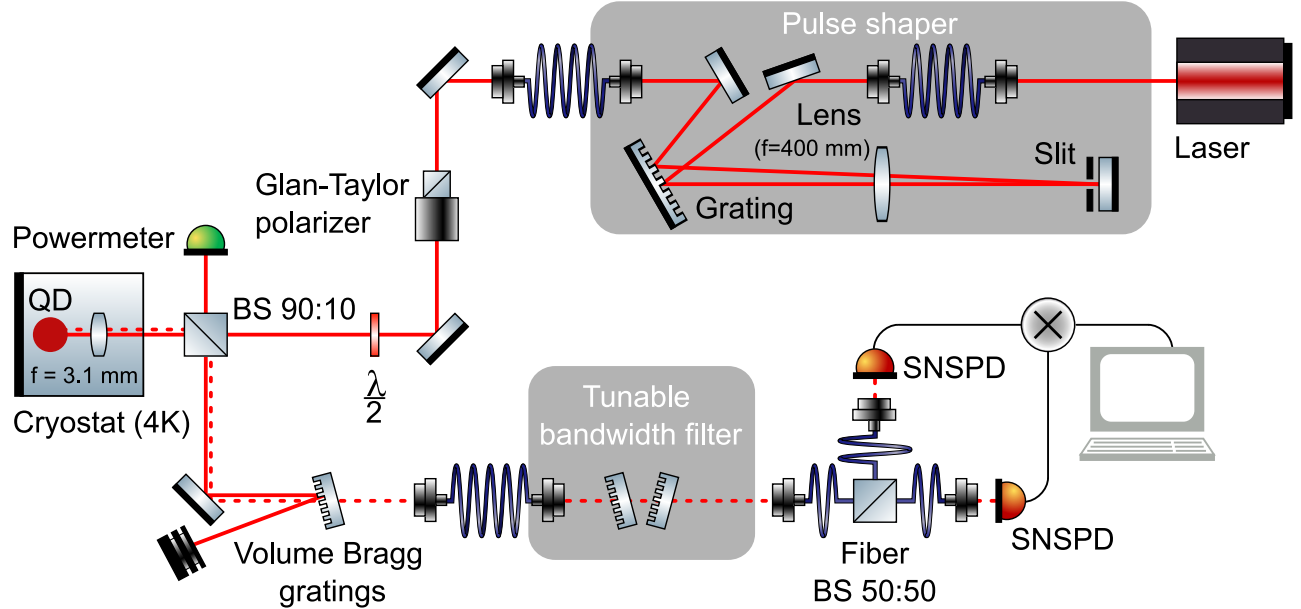


FIG. A1. **Scheme of the experimental setup.** A schematic representation of the main building blocks of the experimental setup, such as excitation pulse laser, pulse shaper, excitation of the QD sample, filtering of the QD transition spectral line and detection. For more detailed setup description see the Appendix A.

beam to linear polarization and the angle of the polarization is then adjustable by a half-wave plate. Just before the cryostat chamber a 90:10 beam splitter cube (BS) is placed to separate the incoming excitation beam and single photons emitted by the QD. Approximately 90 % of the excitation beam (depending in its polarization state) is reflected by the BS to a power meter, which is used to control the QD excitation power, only $\approx 10\%$ on the laser power is guided to the cryostat chamber, where the QD sample is placed.

The sample design [35] features a bottom distributed Bragg reflector where the distance between the 23 pairs of AlAs/GaAs constituting the reflector and the semiconductor/vacuum interface corresponds to a nominal, weak λ cavity, and the QD layer is situated in its anti-node. The attribution of the QD transition to a positive trion, is based on power- and polarization-resolved μ -PL measurements, as well as previous experimental and theoretical investigations [35, 59–61] on similar samples.

The emission is collected by a lens ($f = 3.1$ mm) with an NA of 0.68. The excitation laser suppression is realized on the basis of two volume Bragg grating (VBG) notch filters with blocking a spectral bandwidth (FWHM) 1.2 nm and individual suppression OD6. The QD emission is coupled by a $f = 8$ mm lens collimator. For precise filtering of the QD transition line we use a fiber-coupled bandwidth tunable filter based on VBGs with set filtering spectral bandwidth (FWHM) 150 pm (approximately the QD-transition linewidth).

The full setup exhibits an efficiency of $\eta_{\text{setup}} = 0.15$.

The measurements of $g^{(2)}(\tau)$ are acquired with a fiber-based, symmetric beam splitter in a Hanbury-Brown and Twiss configuration using superconducting nanowire single-photon detectors (SNSPDs) with an efficiency of $\eta_d = 0.86$ each and a time tagging device. The detection exhibits a temporal resolution (FWHM of the system response function) of 34 ps.

APPENDIX B: EVALUATION OF TIME TAGS

For each laser detuning and pump power, a single measurement run is performed from which both the brightness B and purity P are inferred. To obtain enough statistics in the auto-correlation data, each measurement is stopped once the coincidence counts of the uncorrelated side peaks exceed a threshold value (here, 700 counts at 100 ps bin width).

Simply summing the count rates of both detection channels results in probabilistic double-counting of multi-photon states

$$\tilde{B} = B + \sum_{k \geq 2} p_k \left(1 - \frac{1}{2^{k-1}} \right) = B + \frac{1}{2} p_2 + \frac{3}{4} p_3. \quad (\text{B1})$$

Thus, to avoid over-counting we subtract all coincidence events occurring within one repetition period $T_{\text{rep}} = \frac{1}{\nu_{\text{rep}}}$

such that the measured brightness reads as

$$B = \frac{1}{\nu_{\text{rep}}} \frac{1}{\eta_{\text{setup}} \eta_{\text{d}}} \times \left(R_1 + R_2 - CC_{1,2}(t_{\text{coinc}} = 1/\nu_{\text{rep}}) \right) \quad (\text{B2})$$

where R_i is the raw count rate of the i -th detector and CC denotes the coincidence count rate.

The auto-correlation measurements (compare Fig. 1) use a bin width of 100 ps and are numerically evaluated to deduce $g^{(2)}(0)$. We only apply a background subtraction based on the expected coincidences arising from a dark count in at least one of the channels computed as

$$CC_{1,2}^{\text{d}} = R_1 R_2^{\text{d}} + R_2 R_1^{\text{d}} + R_1^{\text{d}} R_2^{\text{d}} \quad (\text{B3})$$

where the superscript 'd' denotes the dark count rates.

Integrating the area over the central repetition period and dividing by the averaged and blinking-corrected area of the outer peaks then yields the $g^{(2)}(0)$ value. For applications in quantum communication, it is crucial to consider the full repetition period when calculating the source's purity since an adversary has access to all the information leaving the sender's lab.

APPENDIX C: PARAMETER ESTIMATION FOR QUANTUM KEY DISTRIBUTION WITH QUANTUM DOTS

1. Practical secure key rate

When assessing the performance of a QKD network, it is necessary to estimate the fraction of securely exchanged qubits, or *untagged*, in order to separate them from the *tagged* qubits where some information could have been leaked. This step, called parameter estimation, will determine the amount of necessary privacy amplification and will therefore be crucial to guarantee practical information-theoretic security. In discrete-variable photonic implementations, the most widely used security proofs assume some form of active (or passive) phase randomization [62], in order to separate the contributions from different photon number components. For LA-excited QDs, it is a fair assumption that the emitted photon states bear very little coherence between the photon-number states [41]. We may then proceed assuming that only the single photons states contribute positively to the secure-key generation, whereas multi-photon states carry redundantly encoded information which could be extracted with Photon Number Splitting (PNS) attacks for instance [63].

We start by briefly recalling some relevant quantities in a practical BB84 QKD scenario. Let us define the yield of a k -photon state as the conditional probability of a detection on the receiver's detector given that the sender generates a k -photon state:

$$Y_k = Y_0 + (1 - Y_0) [1 - (1 - \eta_{\text{d}} \eta_{\text{ch}})^k], \quad (\text{C1})$$

where η_{d} is the detection efficiency, η_{ch} is the channel transmission, and Y_0 is the dark-count probability. We define the gain Q_k of a k -photon state as the probability of a detection event resulting from this state

$$Q_k = p_k Y_k. \quad (\text{C2})$$

where p_k is the probability of k -photon emission from the QD source. Further, we define e_k , the error rate of the k -photon state, as

$$e_k = \frac{e_0 Y_0 + e_{\text{d}} [1 - (1 - \eta_{\text{d}} \eta_{\text{ch}})^k]}{Y_k}, \quad (\text{C3})$$

where the parameter e_{d} characterizes the detection error probability, dependent on the optical alignment of the entire system, and e_0 is the error rate of the background, which, if we assume to be random, is $e_0 = \frac{1}{2}$. In a QKD implementation, the receiver measures the total gain of the signal state Q_{tot}

$$Q_{\text{tot}} = \sum_{k=1}^{\infty} Q_k \quad (\text{C4})$$

and the qubit error rate e_{tot}

$$e_{\text{tot}} = \frac{1}{Q_{\text{tot}}} \sum_{k=1}^{\infty} e_k Q_k \quad (\text{C5})$$

and, after estimating the single-photon gain Q_1 and error e_1 , compute the rate of secure key bits per pulse (SK) with the GLLP formula [49]

$$SK = \frac{1}{2} [Q_1(1 - H_2(e_1)) - f(e_{\text{tot}})Q_{\text{tot}}H_2(e_{\text{tot}})]. \quad (\text{C6})$$

In this formula, the term $f(e_{\text{tot}})Q_{\text{tot}}H_2(e_{\text{tot}})$ accounts for the cost of error correction - $f(e_{\text{tot}})$ being the error correcting code inefficiency and $H_2(\cdot)$ the binary entropy - and $Q_1(1 - H_2(e_1))$ states that only the error-free single photon states contribute to the secure key generation.

Eqs. C1 and C3 describe theoretical values, thus we will now describe two different procedures to estimate e_1 and Q_1 from experimentally accessible quantities.

2. Estimation of single-photon parameters based on auto-correlation functions

We will estimate the multi-photon contribution relying only on the brightness B and single photon purity P . Such quantities are indeed the main source parameters, and are readily measured by the sender. However, since the channel parameters are untrusted, the honest parties have to assume that all losses and errors arise from single photon states, that is $Y_k = 1$ and $e_k = 0$ for $k \geq 2$.

Thus, the single photon parameters can be estimated as follows:

$$Q_1 \geq Q_{\text{tot}} - p_{\text{m}} - Y_0 p_0 \quad (\text{C7})$$

$$e_1 \leq \frac{e_{\text{tot}} Q_{\text{tot}} - \frac{1}{2} Y_0 p_0}{Q_1}, \quad (\text{C8})$$

where $p_0 = 1 - B$ and $p_m = \sum_{k \geq 2} p_k$ is the multi-photon probability. Note that, implicit in the above equations, is the assumption that parties have a trusted estimation of the vacuum contribution. We bound p_m starting from the second-order auto-correlation function, along with the reasonable assumptions that $p_{n \geq 4} = 0$ and $p_1 > p_m$,

$$g^{(2)}(0) = \frac{2p_2 + 6p_3}{(p_1 + 2p_2 + 3p_3)^2} = \frac{2p_m + 4p_3}{(p_1 + 2p_m)^2} \\ \times \left[1 + \frac{p_3}{p_1 + 2p_m} \right]^{-2} \simeq \frac{2p_m}{(p_1 + 2p_m)^2}, \quad (\text{C9})$$

and then truncate it at the zeroth order in p_3 . Computing the error $F(p_1, p_2, p_3)$ introduced by our approximations on the $g^{(2)}(0)$, we note that $F(p_1, p_2, p_3) > 0$ for all $p_k \in (0, 1)$ with $k = 1, 2, 3$ – proving that the right-hand side of Eq. C9 provides an actual lower bound – and $F(p_1, p_2, 0) = 0$ showing that it holds tight in the limit of vanishing p_3 . Hence, solving for p_m , we obtain

$$p_m \leq \frac{1 - Bg^{(2)}(0) - \sqrt{1 - 2Bg^{(2)}(0)}}{g^{(2)}(0)}, \quad (\text{C10})$$

an estimation valid for any source with sub-Poissonian emission, holding at any distance, and providing an explicit bound which only depends on experimentally accessible parameters.

3. Estimation of single-photon parameters based on decoy states

In the previous scenario, Alice and Bob only exchange signal states to establish a secure shared key. However, this leads to an estimation of single photon parameters that is not tight (Eqs. C7 and C8). As a countermeasure, one can let Alice modulate the intensity of the states she sends, chosen from the set $\{\rho, \nu_1, \nu_2, \dots\}$, in a way that is unknown to the eavesdropper. After the quantum step of the protocol, Alice and Bob can evaluate the total gain and error rate for each state $\{Q_{\text{tot}}^{(i)}, e_{\text{tot}}^{(i)}\}$ and solve the system of equations for $\{Y_k, e_k\}$.

These so-called *decoy* states have been shown to increase the achievable SK drastically for implementations based on attenuated laser pulses [52]. Even though decoy states decrease the sifting efficiency η_{sif} as they cannot contribute to the raw key, a tighter estimation of the single-photon contribution is preferable, especially for large distances.

When working with sub-poissonian sources, the multi-photon component $p_{n \geq 4}$ can be neglected and two decoy states are sufficient to compute the yields and error rates, $\{Y_k, e_k\}$, exactly. This implies that we can use the theoretical formulas in Eqs. C1 and C3.

APPENDIX D: EXTENDED ANALYSIS OF SECURE KEY GENERATION WITH QUANTUM DOTS

1. Maximum QKD-distance approximation from experimental measures

Estimating the maximum attainable communication distance d_{max} for QKD for a given source, has high relevance for practical implementations. However, due to the complexity of Eq. C6, one cannot solve it analytically for the channel transmission η_{ch} but has to resort to numerical methods when an tight approximation is required. On the other hand, even the numerical evaluation of the SK for a given photon-number statistics always involves estimating other protocol parameters such as single-photon detection error, detection efficiency, dark-count probability and error-correction code inefficiency. Therefore, an analytic approximation for d_{max} can be advantageous – especially if the required quantities are easily accessible.

We start by upper bounding Eq. C6 by

$$SK \leq \frac{1}{2} Q_1 (1 - H_2(e_1)) \quad (\text{D1})$$

as the cost for error correction, $f(E_{\text{tot}})Q_{\text{tot}}H_2(e_{\text{tot}})$, is strictly positive. The maximum attainable distance d_{max} is formalized as the minimal channel efficiency η_{ch}^{\min} for which $SK > \delta$ where a threshold of $\delta = 10^{-8}$ is used here. From Eq. D1 follows $SK \rightarrow 0$ if $\frac{1}{2} Q_1 (1 - H_2(e_1)) \rightarrow 0$, or further simplified $Q_1 \rightarrow 0$. Note that $e_1 \rightarrow \frac{1}{2}$ results in a vanishing SK but since $Q_1 \rightarrow 0$ also implies $e_1 \rightarrow \frac{1}{2}$ (see Eq. C4, C5, C7, C8) we focus only on $Q_1 \rightarrow 0$. Inserting Eq. C4 into Eq. C7 and rearranging yields

$$Q_1 = p_m \left(\frac{p_1}{p_m} Y_1 + Y_2 - 1 \right). \quad (\text{D2})$$

Since $p_m \geq 0$ for a realistic source, the expression inside the bracket has to tend to zero to cause $Q_1 \rightarrow 0$. Assuming $Y_0 \ll 1$ we can simplify Eq. C1 to $Y_1 = \eta_{\text{ch}} - Y_0$ and $Y_2 = 2\eta_{\text{ch}} - \eta_{\text{ch}}^2 - Y_0$ such that $Q_1 \geq 0$ entails

$$1 \leq \eta_{\text{ch}} \left(\frac{p_1}{p_m} + 2 - \eta_{\text{ch}} \right) - Y_0 \left(\frac{p_1}{p_m} + 1 \right). \quad (\text{D3})$$

As we are looking for long-distance communication, we use $\eta_{\text{ch}} \ll 1$ and rearrange

$$\eta_{\text{ch}} \geq \frac{1}{\frac{p_1}{p_m} + 2} + Y_0 \frac{\frac{p_1}{p_m} + 1}{\frac{p_1}{p_m} + 2} \geq \frac{1}{\frac{p_1}{p_m} + 2} + Y_0. \quad (\text{D4})$$

The maximum distance at which a secure key can still be generated now corresponds to the minimal channel transmission that satisfies Eq. D4. Therefore, we write

$$\eta_{\text{ch}}^{\min} \approx \frac{1}{\frac{p_1}{p_m} + 2} + Y_0 \quad (\text{D5})$$

and finally, use Eq. C10 and $p_1 = B - p_m$ to re-express the result only in terms of B and $g^{(2)}(0)$ as

$$\eta_{ch}^{\min} \approx \frac{1}{Bg^{(2)}(0)} + Y_0. \quad (D6)$$

$$\frac{1}{1 - Bg^{(2)}(0) - \sqrt{1 - 2Bg^{(2)}(0)}} + 1$$

Since $Bg^{(2)}(0) \ll 1$, we can expand $Bg^{(2)}(0)$ in a Taylor series and truncate after the first order such that

$$\eta_{ch}^{\min} \approx \frac{Bg^{(2)}(0)}{2} + Y_0. \quad (D7)$$

For state-of-the-art technology, we have $Y_0 \ll Bg^{(2)}(0)$ such that one can also dismiss Y_0 in the above equation.

Considering the complexity of Eq. C6, the approximation is strikingly simple and follows directly from the fundamental source parameters. Yet, for a broad parameter range, the results compare well to the numeric solution where Eq. D7 always overestimates the maximum distance. This systematic error is rooted in the approximation's derivation as an upper bound and is primarily caused by disregarding the error correction term of Eq. C6. Typically, the overestimation amounts to 25 – 35 km.

In the following section, we juxtapose the approximation to the numeric results for our source.

2. Photon-number optimization via variable attenuation

In Appendix C we inferred all experimental quantities required to calculate the SK directly from the estimated photon-number populations $\{p_k\}$. To include the variable attenuation, we now model the photon loss first. To this end, we apply

$$\begin{aligned} p_0(\eta_{att}) &= p_0 + p_1(1 - \eta_{att}) + p_m(1 - \eta_{att})^2 \\ p_1(\eta_{att}) &= p_1\eta_{att} + p_m(1 - \eta_{att}^2 - (1 - \eta_{att})^2) \\ p_m(\eta_{att}) &= 1 - p_0(\eta_{att}) - p_1(\eta_{att}) \end{aligned} \quad (D8)$$

where we used $p_2 \gg p_3$ and η_{att} is the probability to transmit a photon. Note that this model is equivalent to a beam splitter with tunable reflectivity. The approach is similar to the one used in Ref. [54].

With the modified set of $\{p_k\}(\eta_{att})$, we proceed as before estimating $Q_1, e_1, Q_{tot}, e_{tot}$ and calculating SK . For each communication distance, we optimize the SK over η_{att} to assess the full potential of a given source. This process resembles the optimizations used to identify the ideal mean-photon number in QKD with weak coherent states [43]. The results are depicted in Fig. A2 where we compare our source to idealized sources and detection.

For the experimental source parameters, we find that the maximum brightness is – by coincidence – very close to the point-wise optimized curve. Hence, reducing the effective brightness ($B_{eff}(\eta_{att}) = p_0(\eta_{att}) + p_1(\eta_{att}) +$

$p_m(\eta_{att})$) will reduce the maximum communication distance and the SK at short distances. However, assuming a brighter source, as in Fig. A2 (b), the results change drastically and the benefit of adjusting the attenuation according to the channel loss becomes clear. The enveloping curve (i.e. point-wise optimized) now features three regions with successively larger exponential decrease in the SK . Up to ~ 75 km, the best SK is achieved without any attenuation, since SK predominantly set by p_1 . The next region is shaped by the continuous balancing of $p_1(\eta_{att})$ and $p_m(\eta_{att})$ to optimize SK . Finally, at around 170 km, further attenuation cannot push the maximum distance anymore as the impact of the dark counts dominates.

We indicate in Fig. A2 (a)-(b) the maximum distance approximation obtained from Eq. D7 where the brightness corresponds to the ideal long-distance brightness. We see that Eq. D7 overestimates the distance by ~ 30 km as discussed above.

To analyze the impact of distinct experimental parameters on the SK , we simulate the results for different purities and dark-count probabilities, Y_0 , while the brightness is always assumed as $B = 100\%$. Only displaying the attenuation-optimized SK for each parameter pair, we see how the position of the first inflection point is influenced by p_m (see Eq. C10 for fixed B and changing $g^{(2)}(0)$) whereas the distance at which the SK curve drops for the second time is determined by both, $p_m(\eta_{att})$ and Y_0 . The two inflection points can readily be associated with different causes for the SK to break down. In the first case, the information leakage due to multi-photon events is too large as to permit the sifting of a secure key from the raw key while in the second case, signal clicks are similarly probable as dark-count clicks at the receiver resulting in a high error probability e_1 .

From the above findings, we conclude that a brighter but similarly pure source, as already available in the C-band [36], increases the SK at short and medium distances but will not allow to reach higher distances. The purity on the other hand, has little effect on the SK for a short channel but improves SK for medium distances and – in combination with the a low dark-count probability – boosts the maximum attainable communication distance d_{max} .

APPENDIX E: TIME FILTERING

In the main text, we showed how tuning the excitation conditions of the LA scheme changes the photon-number populations $\{p_k\}$ of the QD source. In a similar way, temporal filtering can be used to manipulate the photon-number statistics and improve secure key rates of QKD [56, 57]. This technique can be implemented irrespective of the excitation scheme but requires a fast amplitude modulator with sufficient suppression at the sender's site. In the following, we compare the two methods based on our experimental data.

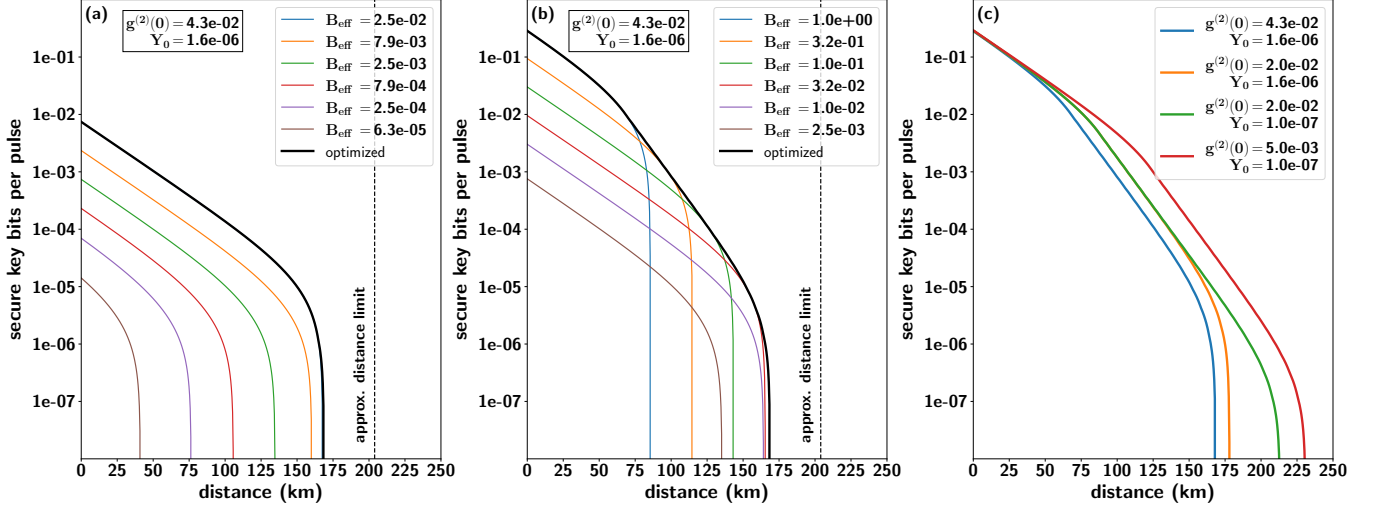


FIG. A2. **Secure key bits per pulse over distance for variable signal attenuation.** Including a variable attenuator into the sender's setup can improve the secure key bits per pulse (SK) at large distances. (a)-(b) The SK as a function of distance is displayed for six effective brightness values, B_{eff} . The thick, black line represents the attainable SK for a point-wise optimization of B_{eff} . The dotted vertical line indicates the approximated maximum distance according to Eq. D7. The dark-count probability $Y_0 = 1.6 \cdot 10^{-6}$ and purity of 95.7% correspond to the experimental data at ideal brightness excitation conditions. For (a) the maximum brightness $B = 2.5\%$ corresponds to the experimental value whereas for (b) an ideal brightness, $B = 100\%$, is assumed. (c) Point-wise optimized curves for a set of $\{g^{(2)}(0), Y_0\}$ highlighting the different influences on the SK . The parameters for all plots are: single-photon detection error $e_d = 0.02$, detection efficiency $\eta_d = 0.86$, error-correction code inefficiency $f = 1.2$, fiber attenuation $\alpha = 0.17 \text{ dB/km}$.

The idea of a temporal filter is to enhance the single-photon purity of the source, and at the same time, reduce the dark-count probability at the receiver. In an experimental realization, the fast amplitude modulator is phase-locked to the driving laser and transmits only during a gating window defined by its widths τ_A and its delay t_0 to the reference input. By adjusting t_0 such that the gating window starts just before the probability of a passing photons peaks (i.e. the peak in the TCSPC measurement), one can vary τ_A to decide how much of the exponential decay trace should be transmitted. While reducing the effective brightness, this technique usually improves the purity by excluding two-photon events caused by refilling, or by reducing the single-photon contribution from neighbouring QDs.

1. Time filtering via post-selection

In this section, we resort to time filtering by post-processing. We, however, emphasize that a secure implementation of time filtering necessarily requires a physical gating of the signal before it is sent through the untrusted channel. Nonetheless, only investigating the potential advantage of time filtering, post-processing yields the same results as a physically gated signal stream.

To mimic this gating using post-selection, we consider only events in the auto-correlation measurement that occur within a post-selection window, $g^{(2)}(0)[\tau_A, t_0 = 0]$,

where τ_A is the tuning parameter. When calculating the resulting $g^{(2)}(0)$ value, we also apply the post-selection window to the n uncorrelated peaks where $t_0 = \pm nT_{\text{rep}}$ (see Appendix B). Furthermore, we compute the corrected brightness as

$$B_{\text{corrected}}(\tau_A) = B \frac{A_{\text{uncorr}}(\tau_A)}{A_{\text{uncorr}}(T_{\text{rep}})} \quad (\text{E1})$$

where A_{uncorr} denotes the average, blinking-corrected area of the uncorrelated peak. Finally, the receiver could choose to disregard signals occurring outside an acceptance window τ_B either by gating the single-photon detectors or by post-processing. To satisfy the security requirements of the parameter estimation (see Appendix C), $\tau_B \geq \tau_A$ must hold. For the following analysis, we set $\tau_B = \tau_A$ and assume the dark counts to be constant in time ($Y_0(t) = Y_0$) such that the time-filtered dark-count probability reads as

$$Y_0(\tau_A) = Y_0 \frac{\tau_A}{T_{\text{rep}}} \quad (\text{E2})$$

2. Time filtering for QKD

Fig. A3 (a)-(b) shows the resulting brightness and purity as function of the window widths τ_A and – for comparison – as function of excitation power. To asses the impact on a QKD implementation, we compute the SK over distance and optimize for the SK by tuning either τ_A or the

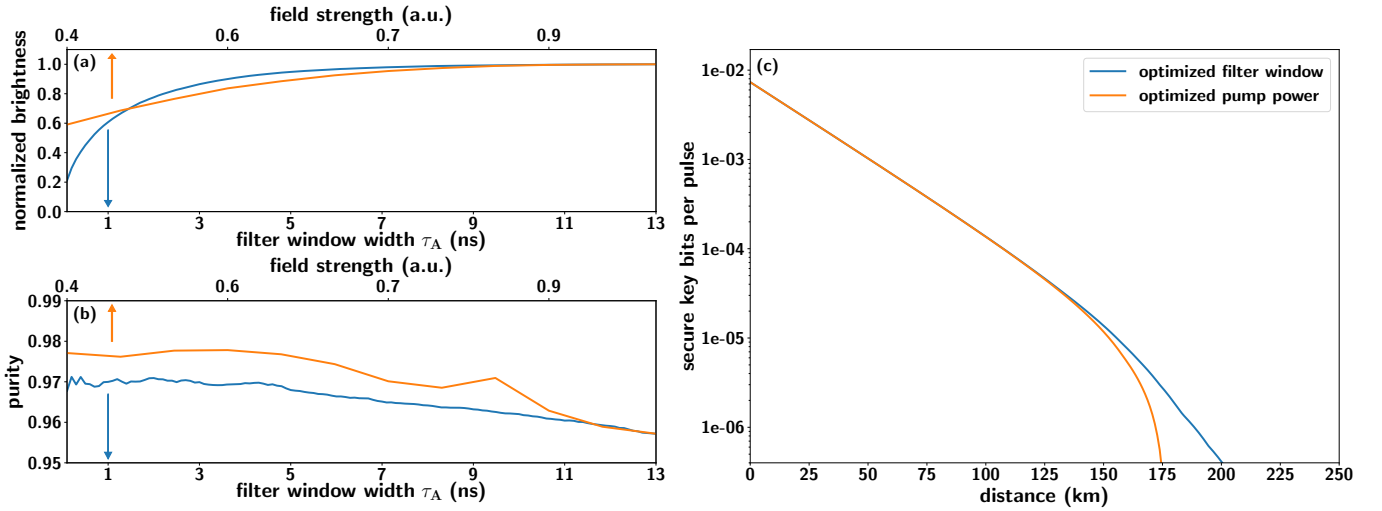


FIG. A3. **Comparing time filtering and pump power tuning for QKD.** Both changing the excitation power or the width of a post-selection window τ_A alter the effective photon-number statistics of the QD source. For a laser detuning of $\Delta\lambda = 1.5$ nm, we analyze their effects in terms of brightness (a), single-photon purity (b) and secure key bits per pulse in a BB84 QKD protocol (c). When the power is chosen as tuning parameter, no time filtering is applied (i.e. $\tau_A = 13.16$ ns), whereas the field strength is set to 1 a.u. when varying τ_A . The parameters for (c) are: single-photon detection error $e_d = 0.02$, detection efficiency $\eta_d = 0.86$, dark-count probability $Y_0 = 1.6 \cdot 10^{-6}$, error-correction code inefficiency $f = 1.2$, fiber attenuation $\alpha = 0.17$ dB/km.

pump power at each step (see Fig. A3 (c)). For simplicity, we restrict the analysis to a fixed detuning $\Delta\lambda = 1.5$ nm.

While both methods perform similar for short to medium distances, we find an improvement of rate at large distances if time filtering is applied. Interestingly, the enhanced *SK* at high loss is attributed not to the improvement of purity but to a reduction of brightness and, even more important, reduction of dark-count probability. For the optimal filter window at 200 km, $\tau_A = 0.2$ ns, the purity is in fact lower than for power-tuning but the simultaneous decrease of dark counts to $Y_0(\tau_A) = 2.4 \cdot 10^{-8}$ – almost two order of magnitudes lower than unfiltered – preponderates. As discussed in Appendix D, the *SK* at long distances is ultimately given by the multi-photon population p_m and dark-count prob-

ability Y_0 where p_m is not just affected by the purity but also the brightness (see Eq. C10).

However, we remark that such a short filter window requires a modulator with > 10 GHz bandwidth and would introduce significant loss at all distances. Alternative routes to decrease Y_0 include the technological advancement of SNSPDs in the long run and – already feasible today – the optimization of their biasing. Reducing the bias current (or voltage, depending on the model) of the SNSPDs affects the detection efficiency but will also lower the dark-count probability. This approach is especially appealing for long-distance communication and can be employed in combination with the power and detuning optimization of photon-number statistics in LA excitation.

[1] Martín-López, E. *et al.* Experimental realization of shor’s quantum factoring algorithm using qubit recycling. *Nat. Photonics* **6**, 773–776 (2012). URL <https://www.nature.com/articles/nphoton.2012.259>.

[2] Saggio, V. *et al.* Experimental quantum speed-up in reinforcement learning agents. *Nature* **591**, 229–233 (2021). URL <https://doi.org/10.1038/s41586-021-03242-7>.

[3] Centrone, F., Kumar, N., Diamanti, E. & Kerenidis, I. Experimental demonstration of quantum advantage for NP verification with limited information. *Nat. Commun.* **12** (2021). URL <https://doi.org/10.1038/s41467-021-21119-1>.

[4] Xu, F., Ma, X., Zhang, Q., Lo, H.-K. & Pan, J.-W. Secure quantum key distribution with realistic devices. *Rev. Mod. Phys.* **92**, 025002 (2020). URL <https://link.aps.org/doi/10.1103/RevModPhys.92.025002>.

[5] Bedington, R., Arrazola, J.-M. & Ling, A. Progress in satellite quantum key distribution. *npj Quantum Inf.* **3**, 30 (2017). URL <https://doi.org/10.1038/s41534-017-0031-5>.

[6] Boaron, A. *et al.* Secure quantum key distribution over 421 km of optical fiber. *Phys. Rev. Lett.* **121**, 190502 (2018). URL <https://link.aps.org/doi/10.1103/PhysRevLett.121.190502>.

[7] Neves, S. *et al.* Experimental cheat-sensitive quantum weak coin flipping. *Nat. Commun.* **14**, 1855 (2023). URL

<https://doi.org/10.1038/s41467-023-37566-x>.

[8] Berlín, G. *et al.* Experimental loss-tolerant quantum coin flipping. *Nat. Commun.* **2**, 561 (2011). URL <https://doi.org/10.1038/ncomms1572>.

[9] Pappa, A. *et al.* Experimental plug and play quantum coin flipping. *Nat. Commun.* 3717. URL <https://doi.org/10.1038/ncomms4717>.

[10] Bozzio, M. *et al.* Experimental investigation of practical unforgeable quantum money. *npj Quantum Inf.* **4**, 5 (2018). URL <https://doi.org/10.1038/s41534-018-0058-2>.

[11] Guan, J.-Y. *et al.* Experimental preparation and verification of quantum money. *Phys. Rev. A* **97**, 032338 (2018). 1709.05882.

[12] Kent, A., Lowndes, D., Pitalúa-García, D. & Rarity, J. *npj Quantum Inf.* **8** (2022). URL <https://doi.org/10.1038/2Fs41534-022-00524-4>.

[13] Ng, S. K., N. Huei Y. and Joshi, Chen Ming, C., Kurt-siefer, C. & Wehner, S. Experimental implementation of bit commitment in the noisy-storage model. *Nat. Commun.* **3** (2012).

[14] Lunghi, T. *et al.* Experimental bit commitment based on quantum communication and special relativity. *Phys. Rev. Lett.* **111**, 180504 (2013). URL <https://link.aps.org/doi/10.1103/PhysRevLett.111.180504>.

[15] Liu, Y. *et al.* Experimental unconditionally secure bit commitment. *Phys. Rev. Lett.* **112**, 010504 (2014). URL <https://link.aps.org/doi/10.1103/PhysRevLett.112.010504>.

[16] Kimble, H. J. The quantum internet. *Nature* **453**, 1023–1030 (2008). URL <https://doi.org/10.1038/2Fnature07127>.

[17] Ren, J.-G. *et al.* Ground-to-satellite quantum teleportation. *Nature* **549**, 70–73 (2017). URL <https://doi.org/10.1038/2Fnature23675>.

[18] Ma, X.-S. *et al.* Quantum teleportation over 143 kilometres using active feed-forward. *Nature* **489**, 269–273 (2012). URL <https://doi.org/10.1038/nature11472>.

[19] Hensen, B. *et al.* Loophole-free bell inequality violation using electron spins separated by 1.3 kilometres. *Nature* **526**, 682–686 (2015). URL <https://doi.org/10.1038/nature15759>.

[20] Ritter, S. *et al.* An elementary quantum network of single atoms in optical cavities. *Nature* **484**, 195–200 (2012). URL <https://doi.org/10.1038/2Fnature11023>.

[21] Wang, H. *et al.* Towards optimal single-photon sources from polarized microcavities. *Nat. Photon.* **13**, 770–775 (2019). URL <http://www.nature.com/articles/s41566-019-0494-3>.

[22] Basso Basset, F. *et al.* Entanglement Swapping with Photons Generated on Demand by a Quantum Dot. *Phys. Rev. Lett.* **123**, 160501 (2019). URL <https://doi.org/10.1103/PhysRevLett.123.160501> <https://link.aps.org/doi/10.1103/PhysRevLett.123.160501>.

[23] Zopf, M. *et al.* Entanglement Swapping with Semiconductor-Generated Photons Violates Bell's Inequality. *Phys. Rev. Lett.* **123**, 160502 (2019). URL <https://doi.org/10.1103/PhysRevLett.123.160502> <https://link.aps.org/doi/10.1103/PhysRevLett.123.160502>.

[24] Tomm, N. *et al.* A bright and fast source of coherent single photons. *Nat. Nanotechnol.* (2021). URL <https://doi.org/10.1038/s41565-020-00831-x>.

[25] Zhai, L. *et al.* Quantum interference of identical photons from remote GaAs quantum dots. *Nature Nanotechnology* **17**, 829–833 (2022). URL <https://www.nature.com/articles/s41565-022-01131-2>.

[26] Anderson, M. *et al.* Quantum teleportation using highly coherent emission from telecom c-band quantum dots. *npj Quantum Inf.* **6**, 14 (2020). URL <https://doi.org/10.1038/s41534-020-0249-5>.

[27] Basset, F. B. *et al.* Quantum teleportation with imperfect quantum dots. *npj Quantum Inf.* **7**, 7 (2021). URL <https://doi.org/10.1038/s41534-020-00356-0>.

[28] Lodahl, P. Quantum-dot based photonic quantum networks. *Quantum Science and Technology* **3**, 013001 (2017). URL <https://doi.org/10.1088/2058-9565/aa91bb>.

[29] Liao, S. K. *et al.* Long-distance free-space quantum key distribution in daylight towards inter-satellite communication. *Nat. Photon.* **11**, 509–513 (2017). URL <http://www.nature.com/doifinder/10.1038/nphoton.2017.116>.

[30] Wang, J., Sciarrino, F., Laing, A. & Thompson, M. G. Integrated photonic quantum technologies. *Nat. Photon.* **14**, 273–284 (2020). URL <http://dx.doi.org/10.1038/s41566-019-0532-1> <http://www.nature.com/articles/s41566-019-0532-1>.

[31] Miyazawa, T. *et al.* Single-photon emission at $1.5 \mu m$ from an InAs/InP quantum dot with highly suppressed multi-photon emission probabilities. *Applied Physics Letters* **109**, 132106 (2016). URL <http://dx.doi.org/10.1063/1.4961888> <http://aip.scitation.org/doi/10.1063/1.4961888>.

[32] Anderson, M. *et al.* Gigahertz-Clocked Teleportation of Time-Bin Qubits with a Quantum Dot in the Telecommunication C Band. *Physical Review Applied* **13**, 054052 (2020). URL <https://doi.org/10.1103/PhysRevApplied.13.054052> <https://link.aps.org/doi/10.1103/PhysRevApplied.13.054052>.

[33] Shooter, G. *et al.* 1GHz clocked distribution of electrically generated entangled photon pairs. *Optics Express* **28**, 36838 (2020). URL <https://opg.optica.org/abstract.cfm?URI=oe-28-24-36838>.

[34] Lettner, T. *et al.* Strain-Controlled Quantum Dot Fine Structure for Entangled Photon Generation at 1550 nm. *Nano Letters* **21**, 10501–10506 (2021). URL <https://pubs.acs.org/doi/10.1021/acs.nanolett.1c04024>.

[35] Sittig, R. *et al.* Thin-film InGaAs metamorphic buffer for telecom C-band InAs quantum dots and optical resonators on GaAs platform. *Nanophotonics* **11**, 1109–1116 (2022). URL <https://www.degruyter.com/document/doi/10.1515/nanoph-2021-0552/html>. 2107.13371.

[36] Nawrath, C. *et al.* High emission rate from a purcell-enhanced, triggered source of pure single photons in the telecom c-band (2022). URL <https://arxiv.org/abs/2207.12898>.

[37] van Leent, T. *et al.* Long-distance distribution of atom-photon entanglement at telecom wavelength. *Phys. Rev. Lett.* **124**, 010510 (2020). URL <https://link.aps.org/doi/10.1103/PhysRevLett.124.010510>.

[38] Thomas, S. E. *et al.* Bright polarized single-photon source based on a linear dipole. *Phys. Rev. Lett.* **126**, 233601 (2021). URL <https://link.aps.org/doi/10.1103/PhysRevLett.126.233601>.

[39] Reindl, M. *et al.* Phonon-assisted two-photon interference from remote quantum emitters. *Nano Lett.* **17**, 4090–4095 (2017). URL <http://dx.doi.org/10.1021>

acs.nanolett.7b00777.

[40] Reindl, M. *et al.* Highly indistinguishable single photons from incoherently excited quantum dots. *Physical Review B* **100** (2019). URL <https://doi.org/10.1103/physrevb.100.155420>.

[41] Bozzio, M. *et al.* Enhancing quantum cryptography with quantum dot single-photon sources. *npj Quantum Inf.* **8**, 104 (2022). URL <https://doi.org/10.1038/2Fs41534-022-00626-z>.

[42] Cosacchi, M., Ungar, F., Cygorek, M., Vagov, A. & Axt, V. M. Emission-frequency separated high quality single-photon sources enabled by phonons. *Phys. Rev. Lett.* **123**, 017403 (2019). URL <https://link.aps.org/doi/10.1103/PhysRevLett.123.017403>.

[43] Ma, X. Quantum cryptography: theory and practice (2008). 0808.1385.

[44] Quilter, J. H. *et al.* Phonon-assisted population inversion of a single InGaAs/GaAs quantum dot by pulsed laser excitation. *Phys. Rev. Lett.* **114**, 137401 (2015). URL <https://link.aps.org/doi/10.1103/PhysRevLett.114.137401>.

[45] Bounouar, S. *et al.* Phonon-assisted robust and deterministic two-photon biexciton preparation in a quantum dot. *Phys. Rev. B* **91**, 161302 (2015). URL <https://link.aps.org/doi/10.1103/PhysRevB.91.161302>.

[46] Glässl, M., Barth, A. M. & Axt, V. M. Proposed robust and high-fidelity preparation of excitons and biexcitons in semiconductor quantum dots making active use of phonons. *Phys. Rev. Lett.* **110**, 147401 (2013). URL <https://journals.aps.org/prl/abstract/10.1103/PhysRevLett.110.147401>.

[47] Gustin, C. & Hughes, S. Efficient pulse-excitation techniques for single photon sources from quantum dots in optical cavities. *Advanced Quantum Technologies* **3**, 1900073 (2019). URL <https://doi.org/10.1002/qute.201900073>.

[48] Barth, A. M. *et al.* Fast and selective phonon-assisted state preparation of a quantum dot by adiabatic undressing. *Phys. Rev. B* **94**, 045306 (2016). URL <https://link.aps.org/doi/10.1103/PhysRevB.94.045306>.

[49] Gottesman, D., Lo, H.-K., Lütkenhaus, N. & Preskill, J. Security of quantum key distribution with imperfect devices. *Quantum Info. Comput.* **4**, 325–360 (2004).

[50] Hanschke, L. *et al.* Quantum dot single-photon sources with ultra-low multi-photon probability. *npj Quantum Inf.* **4** (2018). URL <https://www.nature.com/articles/s41534-018-0092-0>.

[51] Bennett, C. H. & Brassard, G. Quantum cryptography: Public key distribution and coin tossing. In *Proc. IEEE International Conference on Computers, Systems and Signal Processing*, vol. 1, 175–179 (Bangalore, India, 1984). URL <https://researcher.watson.ibm.com/researcher/files/us-bennetc/BB84highest.pdf>.

[52] Lo, H.-K., Ma, X. & Chen, K. Decoy state quantum key distribution. *Phys. Rev. Lett.* **94**, 230504 (2005). URL <https://link.aps.org/doi/10.1103/PhysRevLett.94.230504>.

[53] Wang, X.-B. Beating the photon-number-splitting attack in practical quantum cryptography. *Phys. Rev. Lett.* **94**, 230503 (2005). URL <https://link.aps.org/doi/10.1103/PhysRevLett.94.230503>.

[54] Waks, E., Santori, C. & Yamamoto, Y. Security aspects of quantum key distribution with sub-poisson light. *Phys. Rev. A* **66**, 042315 (2002). URL <https://link.aps.org/doi/10.1103/PhysRevA.66.042315>.

[55] Grünwald, P. Effective second-order correlation function and single-photon detection. *New Journal of Physics* **21**, 093003 (2019). URL <https://dx.doi.org/10.1088/1367-2630/ab3ae0>.

[56] Ates, S. *et al.* Improving the performance of bright quantum dot single photon sources using temporal filtering via amplitude modulation. *Scientific Reports* **3** (2013). URL <https://doi.org/10.1038/srep01397>.

[57] Kupko, T. *et al.* Tools for the performance optimization of single-photon quantum key distribution. *npj Quantum Inf.* **6**, 29 (2020). URL <https://www.nature.com/articles/s41534-020-0262-8>.

[58] Michler, P. *Single Semiconductor Quantum Dots*. NanoScience and Technology (Springer Berlin Heidelberg, Berlin, Heidelberg, 2009). URL <https://ebookcentral.proquest.com/lib/kxp/detail.action?docID=450865>.

[59] Paul, M. *et al.* Single-photon emission at $1.55 \mu\text{m}$ from MOVPE-grown InAs quantum dots on InGaAs/GaAs metamorphic buffers. *Applied Physics Letters* **111**, 033102 (2017). URL <http://aip.scitation.org/doi/10.1063/1.4993935>.

[60] Carmesin, C. *et al.* Structural and optical properties of InAs/(In)GaAs/GaAs quantum dots with single-photon emission in the telecom C-band up to 77 K. *Physical Review B* **98**, 125407 (2018). URL <https://link.aps.org/doi/10.1103/PhysRevB.98.125407>.

[61] Dusanowski, L. *et al.* Optical charge injection and coherent control of a quantum-dot spin-qubit emitting at telecom wavelengths. *Nat. Commun.* **13**, 748 (2022). URL <https://www.nature.com/articles/s41467-022-28328-2>.

[62] Lo, H.-K. & Preskill, J. Security of quantum key distribution using weak coherent states with nonrandom phases. *Quantum Info. Comput.* **7**, 431–458 (2007). URL <https://dl.acm.org/doi/10.5555/2011832.2011838>.

[63] Brassard, G., Lütkenhaus, N., Mor, T. & Sanders, B. C. Limitations on practical quantum cryptography. *Phys. Rev. Lett.* **85**, 1330–1333 (2000). URL <https://link.aps.org/doi/10.1103/PhysRevLett.85.1330>.